Archival Report

Biological Psychiatry

The Variegation of Human Brain Vulnerability to Rare Genetic Disorders and Convergence With Behaviorally Defined Disorders

Elizabeth Levitis, Siyuan Liu, Ethan T. Whitman, Allysa Warling, Erin Torres, Liv S. Clasen, François M. Lalonde, Joelle Sarlls, Daniel C. Alexander, and Armin Raznahan

ABSTRACT

BACKGROUND: Diverse gene dosage disorders (GDDs) increase risk for psychiatric impairment, but characterization of GDD effects on the human brain has so far been piecemeal, with few simultaneous analyses of multiple brain features across different GDDs.

METHODS: Here, through multimodal neuroimaging of 3 aneuploidy syndromes (XXY [total n = 191, 92 control participants], XYY [total n = 81, 47 control participants], and trisomy 21 [total n = 69, 41 control participants]), we systematically mapped the effects of supernumerary X, Y, and chromosome 21 dosage across a breadth of 15 different macrostructural, microstructural, and functional imaging–derived phenotypes (IDPs).

RESULTS: The results revealed considerable diversity in cortical changes across GDDs and IDPs. This variegation of IDP change underlines the limitations of studying GDD effects unimodally. Integration across all IDP change maps revealed highly distinct architectures of cortical change in each GDD along with partial coalescence onto a common spatial axis of cortical vulnerability that is evident in all 3 GDDs. This common axis shows strong alignment with shared cortical changes in behaviorally defined psychiatric disorders and is enriched for specific molecular and cellular signatures.

CONCLUSIONS: Use of multimodal neuroimaging data in 3 aneuploidies indicates that different GDDs impose unique fingerprints of change in the human brain that differ widely depending on the imaging modality that is being considered. Embedded in this variegation is a spatial axis of shared multimodal change that aligns with shared brain changes across psychiatric disorders and therefore represents a major high-priority target for future translational research in neuroscience.

https://doi.org/10.1016/j.biopsych.2023.07.008

Gene dosage disorders (GDDs)—including recurrent subchromosomal copy number variations and chromosomal aneuploidies—are individually rare but collectively common risks for neuropsychiatric impairment and model genetic influences on human brain development. However, most neuroimaging studies of GDDs have considered at most only a few imaging-derived phenotypes (IDPs) when comparing different GDDs (1–4). Although neuroanatomical phenotypes have been studied extensively, there has been sparse sampling of other multimodal IDPs in GDDs, which has limited our biological understanding of each GDD and prevented us from determining the full extent of convergence versus divergence in brain changes across different GDDs. Achieving a more comprehensive comparison is important because any detected convergent effects of different GDDs on the brain may represent a biological substrate for the shared capacity of distinct GDDs to increase risk for a common set of behaviorally defined neuropsychiatric disorders such as autism spectrum disorder and attention-deficit/hyperactivity disorder (5).

Here, we detail the regional effects of multiple GDDs on multiple IDPs through multimodal neuroimaging of the 3 most common human aneuploidy syndromes: Klinefelter syndrome (47,XXY); 47,XYY; and Down syndrome (trisomy 21, T21). We focused on these particular GDDs because 1) they are all trisomies involving supernumerary dosage of large and distinct gene sets, 2) they have each been robustly associated with large effect size changes in brain structure and function [XXY (1,6), XYY (7), and T21 (8,9)], and 3) they are important from a medical perspective given their population prevalence [1:576 males XXY, 1:851 males XYY, 1:592 births T21 (10)] and capacity to increase risk for neuropsychiatric and cognitive impairment (5,11).

We examined 15 IDPs in each GDD from T1-weighted structural magnetic resonance imaging (sMRI), diffusion-weighted imaging (DWI), and resting-state functional MRI (rs-fMRI) to advance understanding of genetic effects on the human brain in 3 key directions. First, by generating 15 IDP change (ΔIDP) maps for each GDD group, we substantially

ISSN: 0006-3223

expanded upon the set of brain features that have been studied in human aneuploidies to date. Notably, here and throughout this article, we use the term "change" to refer to anatomical alterations associated with presence of a supernumerary chromosome (rather than longitudinal within-person anatomical changes over time). Second, by comparing all 45 ΔIDP maps (15 in each GDD) with one another, we directly tested competing mechanistic models for the mapping of genetic effects on cortical organization. For example, GDDs may all impact the same set of IDPs but in different cortical regions, or they may impact the same cortical regions but manifest in different IDPs. Third, we combined information across all IDPs to define and characterize the principal spatial component of cortical change in each GDD—as a step toward testing for a potentially shared backbone of multimodal change that is generalizable across multiple GDDs. Finally, we assessed the extent to which shared effects of different GDDs on the brain align with brain changes shared among the many diverse behaviorally defined neuropsychiatric disorders (BDDs) that are seen at elevated rates in GDDs.

METHODS AND MATERIALS

Participants

The current study includes a total of 341 participants ages 6 to 25 years from 3 case-control cohorts: XXY (total n = 191, 92 control participants), XYY (total n = 81, 47 control participants), and T21 (total n = 69, 41 control participants). Participants were recruited through parent support organizations, the National Institute of Mental Health website, and the National Institutes of Health Healthy Volunteer office. All 341 participants had sMRI data available, with subsets of each case-control cohort having DWI (total n = 253; XXY case/control = 83/69; XXY case/control = 21/41; T21 case/control = 25/14) and rs-fMRI data (total n = 244; XXY case/control = 66/73; XYY case/control = 22/42; T21 case/control = 12/29). Participant characteristics are given in Table 1 for the full sample and are broken down by imaging modality in Table S1. All participants had normal radiological reports and no prior brain injuries. Complete information about the T21 sample can be found in Lee *et al.* (8). All XXY and XYY participants were nonmosaic with a genetic diagnosis confirmed by karyotype, and all control participants were screened using a structured interview to exclude a history of neurodevelopmental or psychiatric disorders. This study was approved by the National Institutes of Health Combined Neuroscience Institutional Review Board. All participants gave consent or assent, as appropriate, and all protocols were completed at the National Institutes of Health Clinical Center in Bethesda, Maryland.

Neuroimaging Data Acquisition and Preprocessing

All sMRI (T1-weighted magnetization-prepared rapid acquisition gradient-echo), DWI, and rs-fMRI (10-minute echo-planar imaging for XXY and XYY; 5-minute, 15-second echo-planar imaging for T21) data were gathered using one MR750 3T scanner (General Electric) for XXY and XYY and another GE 3T scanner for T21, with identical sequences within each case-control aneuploidy cohort (Supplement). Each imaging modality was preprocessed as summarized below, with full methods in the Supplement. Modality-specific quality control information is detailed in the Supplement and is summarized in Figure S1.

Structural MRI. We used the Brain Imaging Data Structure–compatible FreeSurfer pipeline version 7.1.0 to process each subject's T1-weighted MRI scan through the automated recon-all processing stream to generate the cortical surface reconstruction from which we measured the following morphometric features for all 360 cortical parcels in the multimodally-derived HCP (Human Connectome Project) regional parcellation (12): mean cortical thickness (CT), total surface area (SA), total gray matter volume (GMV), mean curvature, gaussian curvature, intrinsic curvature index, and folding index. Based on past guidelines, all participants in the current study had an sMRI-derived Euler number > -217 (13), and individual-specific Euler numbers were included in all statistical models as proxies for image quality (see Computing Regional ΔIDP in Each Aneuploidy).

Diffusion-Weighted Imaging. The following partially dissociable (14) voxelwise diffusion tensor imaging metrics were derived through Tractoflow version 2.2.1 (15): fractional anisotropy (FA), geodesic anisotropy, mean diffusivity, radial diffusivity, axial diffusivity, and tensor mode (further detailed in the Supplement).

Table 1. Participant Characteristics for the Total Sample

		XXY		XYY		T21	
Imaging Modality	Sample Characteristics	Case	Control	Case	Control	Case	Control
Structural	Participants, *n*	99	92	34	47	28	41
	Age, Years, Mean (SD)	16.4 (4.8)	16.2 (5.6)	15.5 (5.3)	14.0 (4.7)	15.7 (5.5)	16.9 (5.9)
	Full Scale IQ, Mean (SD)	93.3 (12.2)	115.1 (12.6)	87.1 (12.4)	118.5 (9.8)	53.6 (14.6)	116.3 (15.8)
	SES, Mean (SD)	47.3 (20.6)	37.7 (17.4)	54.9 (18.0)	38.3 (15.4)	41.0 (14.6)	39.2 (21.5)
Diffusion	Participants, *n*	83	69	21	41	14	25
	Age, Years, Mean (SD)	16.3 (4.9)	16.2 (5.4)	16.1 (5.4)	13.9 (4.8)	17.6 (5.4)	17.1 (6.2)
Functional	Participants, *n*	66	73	22	42	12	29
	Age, Years, Mean (SD)	16.9 (4.2)	17.9 (4.8)	17.1 (4.5)	14.7 (4.4)	17.2 (4.7)	18.5 (4.5)

T21 (trisomy 21) cases and controls included both males and females. Socioeconomic status (SES) was measured using the Hollingshead Four Factor Index of Socioeconomic Status. See Table S1 for global measures across all imaging-derived phenotypes and aneuploidies.

Resting-State Functional MRI. All rs-fMRI scans were preprocessed using fMRIPrep version 20.2.0 (16–18) and the eXtensible Connectivity Pipeline (19) to compute 2 voxelwise metrics of local connectivity: regional homogeneity and amplitude of low-frequency fluctuation (ALFF) (further detailed in the Supplement). rs-fMRI data are subject to well-described signal losses in certain areas of the brain (20,21), and we removed 16 of 360 HCP regions of interest (ROIs) from all subsequent analyses based on their missing rs-fMRI data for 20 or more subjects (Figure S9).

Computing Regional ΔIDP in Each Aneuploidy

The preprocessing steps mentioned above generated complete person-specific measures of 15 IDPs for 344 cortical ROIs in each of the 3 case-control cohorts studied (1 for each GDD). These data were used to compute 15 aneuploidy-specific ΔIDP maps per GDD (Figure 1). For each IDP and cohort, we *z* scored each ROI's IDP values across individuals and modeled the effect of group status (case vs. control) on the IDP while controlling for age and total tissue volume (TTV). TTV was included as a covariate in main analyses given the known robust size reductions in XXY and T21 combined with mean TTV increases in XYY (1,8) to protect against the ROI-level GDD comparisons being trivially colored by global effects [especially for ROI sMRI measures that scale closely with TTV (22) but also for TTV-correlated DWI measures (23)]. All analyses were repeated without TTV covariation, as detailed in the Supplement and referred to in the Results. Additional covariates were the Euler number (all IDPs), framewise displacement (rs-fMRI–derived IDPs), and sex (all IDPs in the T21 case-control cohort). Case-control differences were estimated as the standardized beta coefficients (henceforth "effect sizes") for the group effect, and statistically significant regional ΔIDP were identified by applying false discovery rate (FDR) correction to the vectors of 344 *p* values for each GDD-IDP combination.

Defining Organizing Principles of Cortical Change Across IDPs, Regions, and Aneuploidies

We estimated the pairwise similarity between all 45 unthresholded ΔIDP maps (15 IDPs for each of 3 aneuploidies) based on their spatial correlation across all 344 ROIs. The resulting symmetrical 45 × 45 correlation matrix was characterized using 2 complementary approaches. First, we ordered rows and columns using hierarchical clustering based on Euclidean distance to describe the broad structure of this correlation matrix, paying attention to whether ΔIDP groups were organized primarily by modality or aneuploidy type. Second, we used an established spatial permutation framework to identify statistically significant intermap similarities among all 990 unique pairwise comparisons while accounting for spatial autocorrelations within maps and correcting for multiple comparisons (Supplemental Methods) (24,25).

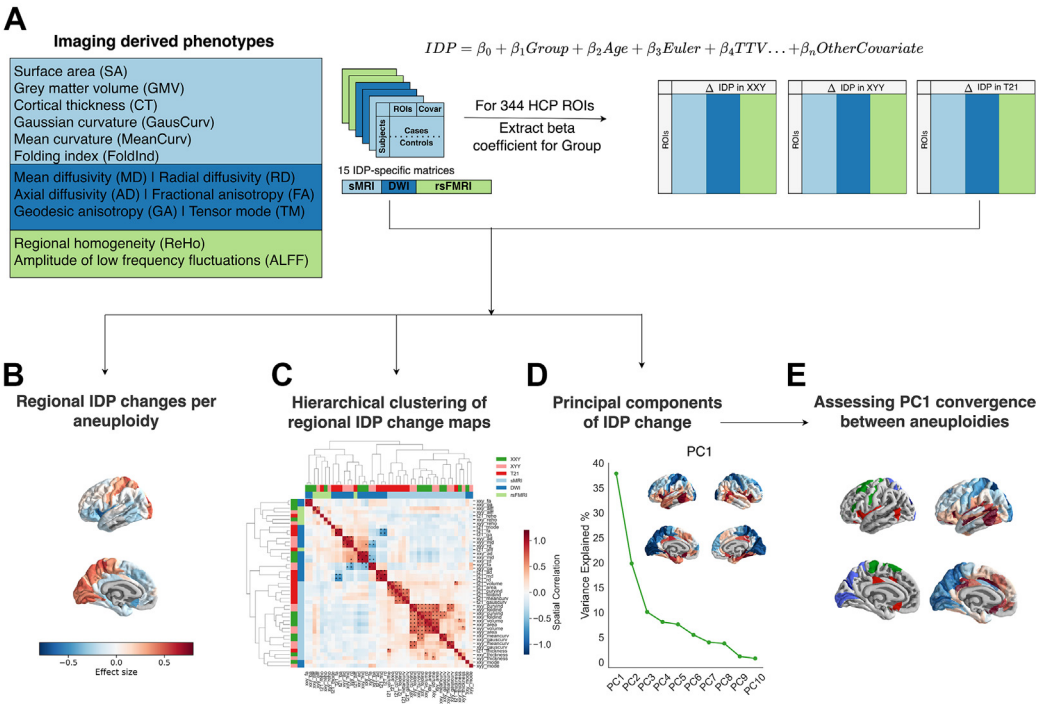

Figure 1. Analytical workflow. **(A)** On the left, we list the phenotypes analyzed for each modality. For each aneuploidy separately, we model each standardized phenotype as a function of group, age, Euler number, total tissue volume, and aneuploidy + modality-specific covariates. The group effect is extracted for each region of interest (ROI) and phenotype to yield a 344 ROI × 15 imaging-derived phenotype change (ΔIDP) matrix per disorder. We **(B)** visualize the individual disorder-ΔIDP maps, **(C)** perform hierarchical clustering on a cross-disorder concatenated 344 × 45 matrix, **(D)** apply principal component (PC) analysis to each disorder's ROI × ΔIDP matrix separately to identify patterns of multimodal change, and **(E)** assess PC1 convergence across aneuploidies continuously and discretely. DWI, diffusion-weighted imaging; HCP, Human Connectome Project; rs-FMRI, resting-state functional magnetic resonance imaging; sMRI, structural magnetic resonance imaging.

Defining and Characterizing Principal Components of Multimodal Cortical Change in Each Aneuploidy

We used principal component analysis (PCA) to provide a summary representation of multimodal change for each aneuploidy, defined by ROI scores for the first principal component (PC1) of the 344 × 15 ΔIDP matrix and associated feature loadings for this PC. We compared PC1s between aneuploidies using cross-ROI spatial correlations in PC1 scores and cross-IDP correlations in feature loadings. To aid cross-aneuploidy comparisons, the polarity of these first PCs were set to maximize positive interaneuploidy PC1 map correlation. We focused our main analyses on PC1, but maps of ROI scores and IDP loadings are provided for the first 5 PCs in each aneuploidy (explaining a cumulative variance >80%) in the Supplement. We also examined convergence between aneuploidy PC1 maps using a conjunction analysis (Supplement) and put PC1 into broader biological context by comparison with canonical maps of cortical function and histology (26–28) (Supplement).

Assessing Spatial Alignment With the PC of Morphometric Change in Behaviorally Defined Psychiatric Disorders

The ENIGMA (Enhancing Neuro Imaging Genetics through Meta Analysis) toolbox (29) contains case-control maps for CT and SA data across 68 brain regions defined using the Desikan-Killiany parcellation (Supplement). Available case-control maps included the following: a CT map for autism spectrum disorder; CT and SA maps for pediatric, adolescent, and adult populations with attention-deficit/hyperactivity disorder; CT and SA maps for adolescent and adult populations with bipolar disorder; CT and SA maps for adolescent and adult populations with major depressive disorder; CT and SA maps for pediatric and adult obsessive-compulsive disorder populations; and CT and SA maps for schizophrenia. We collated these 21 case-control maps and applied PCA to identify PC1 (ENIGMA-PC1) of morphometric change. To enable comparison of the spatial alignment between the ENIGMA-PC1 map with the average PC1 map across XXY, XYY, and T21 (Aneuploidy-PC1), we mapped the HCP ROIs onto the FreeSurfer 5 cortical surface vertices and averaged the PC1 vertexwise scores across the Desikan-Killiany ROIs. Then, we computed the Pearson correlation between the ENIGMA-PC1 and Aneuploidy-PC1 maps and performed a spin test to assess significance.

Gene Category Enrichment Analysis of the Cross-Disorder Aneuploidy Map

We used the Allen Human Brain Atlas to compute gene expression for 15,633 genes across the HCP-Glasser brain regions and perform gene category enrichment analysis of the Aneuploidy-PC1 map (Supplement).

RESULTS

Expanding the Neuroimaging Phenotypes of Aneuploidy Syndromes

For each aneuploidy, ΔIDP maps were visualized as unthresholded effect size maps (Figure 2A, left hemisphere and Figure S2A, both hemispheres) and thresholded maps after FDR correction for multiple comparisons across regions (Figure S2B, both hemispheres). See Table S2 for effect sizes and FDR-corrected q values computed with and without TTV correction.

For all 3 aneuploidies, our findings for GMV, SA, and CT replicated those of previous reports (1,8). For XXY and XYY, we observed GMV and SA changes in bilateral frontotemporal (reductions) and occipitoparietal cortices (increases) as well as CT changes in temporoinsular (reductions) and somatosensory cortices (increases). For T21, we observed occipitoparietal and somatosensory increases in GMV that were recapitulated by changes in CT, while frontotemporal reductions in GMV were recapitulated by changes in SA. By detailing aneuploidy effects on sMRI-derived measures of cortical curvature, we found widespread changes in cortical folding which echoed SA changes in each aneuploidy, suggesting that atypical gyrification is likely a key mediator of genetic effects on SA.

Examining effect size maps for DWI and rs-fMRI–derived IDPs enabled us to expand understanding of regional cortical vulnerability to aneuploidy beyond the more commonly studied morphometric features captured by sMRI. For example, across the diffusion tensor imaging–derived IDPs, FA alterations followed a rostrocaudal gradient in XYY (decreasing rostrally, increasing caudally) and a ventrodorsal gradient in XXY (decreasing dorsally, increasing ventrally), whereas FA showed subthreshold global increases in T21. Diffusivity measures also showed regionally patterned alterations that varied between aneuploidies and differed from FA changes. Changes in rs-fMRI–derived IDPs were also regionally specific in a manner that varied for ALFF and regional homogeneity as well as across the aneuploidies. For example, ALFF was decreased in the inferior frontal cortex of both XXY and XYY, while in XXY it was also decreased in the medial prefrontal cortices and the anterior and posterior cingulate. In contrast, ALFF showed large effect size parietofrontal decreases and lateralized insular increases in T21. The robust effect size of T21 for most sMRI-derived IDPs (Figure 2A) combined with the lack of statistically significant effects for DWI- and rs-fMRI–derived metrics is consistent with the reduced sample size for these 2 modalities compared with that for sMRI in T21, a phenomenon which also applies to XYY and XXY cohorts and encourages cross-IDP visual comparisons using effect size maps (Figure 2A) rather than thresholded maps alone (Figure S2B). Nevertheless, qualitative comparison of both unthresholded (Figure 2A) and thresholded (Figure S2B) ΔIDP maps indicates that inclusion of DWI- and rs-fMRI–derived phenotypes identified additional regional effects of aneuploidy on the brain that were not detected using only sMRI-derived phenotypes.

Defining Organizing Principles of Cortical Change Across IDPs, Regions, and Aneuploidies

Hierarchical clustering of all 45 ΔIDP maps (15 maps for each of 3 aneuploidies) revealed that similarities between ΔIDP maps were most strongly organized by imaging modality and then by aneuploidy type (Figure 2B). For example, at the 3-cluster level, ΔIDP maps were grouped into a large cluster of predominantly sMRI-based ΔIDP maps (e.g., CT, SA, GMV, folding index, gaussian curvature, mean curvature) from all 3

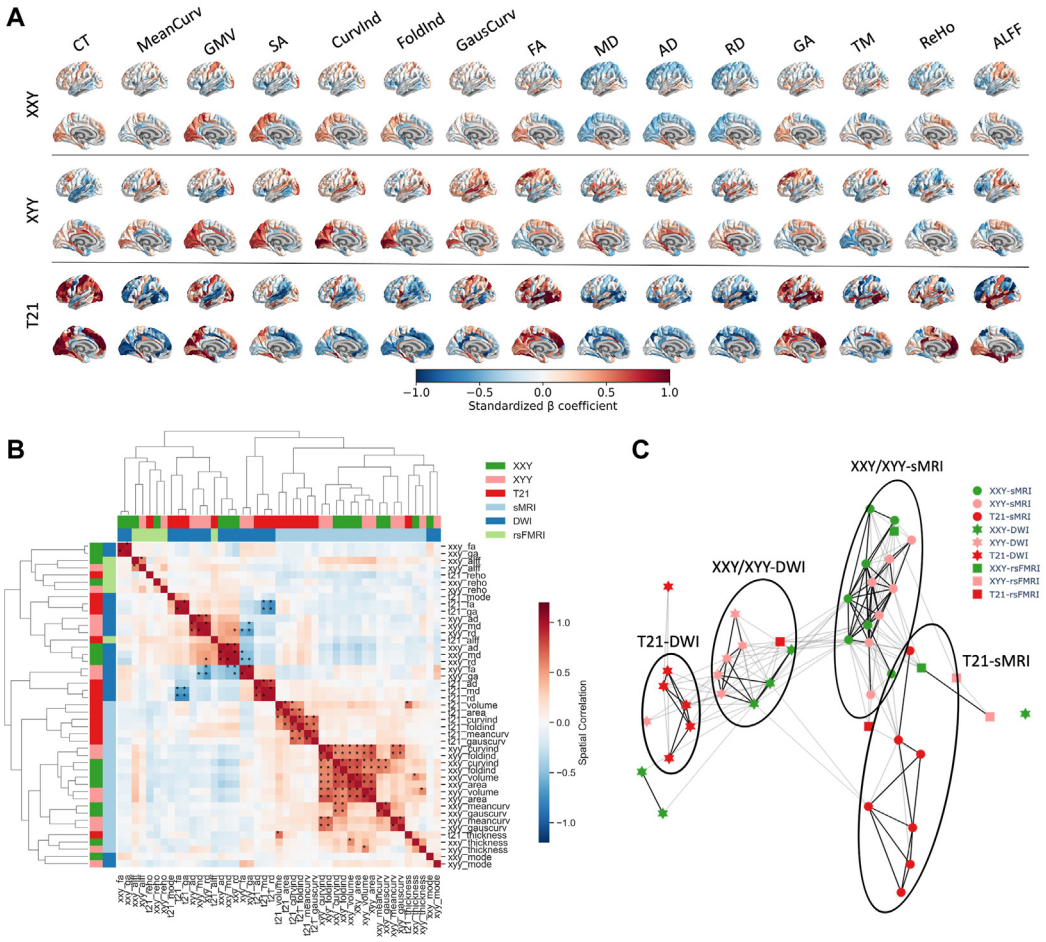

Figure 2. The spatial patterning of cortical change for 15 imaging-derived phenotypes (IDPs) in 3 aneuploidies. **(A)** Unthresholded effect size maps of IDP change (i.e., ΔIDP maps) for each aneuploidy (left hemisphere only; see Figure S2A for right hemisphere). Positive beta values reflect increases in cases relative to controls for a particular IDP of interest whereas negative beta values correspond to decreases in cases relative to controls. **(B)** Hierarchical clustering matrix of all 45 ΔIDP maps. Asterisks denote a significant spatial correlation between maps that survived correction using a strict null based on random spatial rotation (spinning) of maps. **(C)** A force-directed graphical representation of the relationship among all ΔIDP maps. Nodes represent ΔIDP maps, with color encoding the aneuploidy of origin and shape encoding imaging modality (squares, rs-fMRI; circles, T1-weighted; stars, diffusion tensor imaging). Edges represent the spatial correlation between ΔIDP maps, with edge width encoding the absolute Pearson *r* between maps across cortical regions of interest and black edges being are statistically significant. Ellipses have been added to show the separation between T21-DWI nodes, XXY/XYY-DWI nodes, XXY/XYY-sMRI nodes, and T21-sMRI nodes from left to right. AD, axial diffusivity; ALFF, amplitude of low-frequency fluctuation; CT, cortical thickness; CurvInd, intrinsic curvature index; DWI, diffusion-weighted imaging; FA, fractional anisotropy; FoldInd, folding index; GA, geodesic anisotropy; GausCurv, gaussian curvature; GMV, gray matter volume; MD, mean diffusivity; MeanCurv, mean curvature; RD, radial diffusivity; ReHo, regional homogeneity; rs-fMRI, resting-state functional magnetic resonance imaging; SA, total surface area; sMRI, structural magnetic resonance imaging; TM, tensor mode.

aneuploidies, and 2 clusters were mostly made up of DWI- and rs-fMRI–based features—one dominated by ΔIDP maps for diffusivity, anisotropy, regional homogeneity, and ALFF measures, and the other including T21 diffusivity and XYY anisotropy ΔIDP maps. The correlational structure within each of these clusters appeared to primarily (but not exclusively) distinguish the spatial patterns of cortical changes in T21 from those in XXY and XYY. Thus, the dominant and secondary sources of variation in the spatial pattern of cortical change appear to be the imaging modality and specific aneuploidy being considered, respectively. This conclusion was also supported when only considering the statistically significant (24,25) pairwise similarities between ΔIDP maps (asterisked in Figure 2B) and visualizing these in a force-directed graph (Figure 2C).

Defining and Characterizing PCs of Multimodal Cortical Change Within and Across Aneuploidies

We used PCA to provide a summary representation of multimodal change for each aneuploidy, defined by ROI scores for PC1 of the aneuploidy's 344 × 15 ΔIDP matrix and associated feature loadings for this PC. The 3 PC1 maps explained 38%, 31%, and 25% of the variance in XXY, XYY, and T21 ROI × ΔIDP matrices, respectively (Figure 3A). The spatial distribution of regional PC1 scores showed some

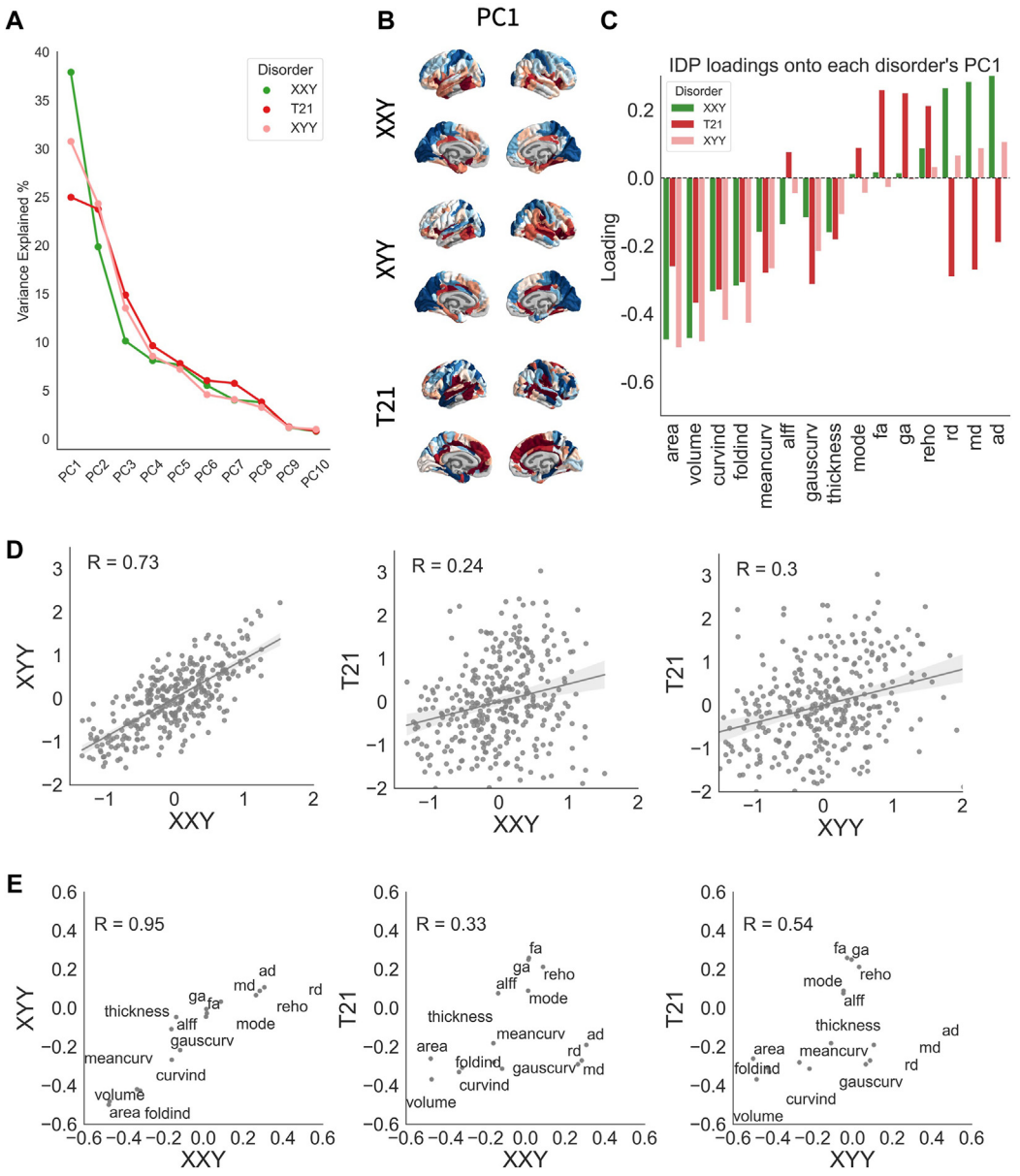

Figure 3. Defining and comparing the principal component (PC) of cortical change in each aneuploidy. **(A)** Proportion of variance explained by the top 10 PCs of each aneuploidy's region of interest × imaging-derived phenotype change (ΔIDP) matrix. **(B)** Region of interest PC1 scores for each aneuploidy projected onto the surface of the brain. **(C)** IDP loadings for each aneuploidy's PC1. **(D)** Correlation between regional PC1 scores for each pair of aneuploidies. **(E)** Correlation between PC1 IDP loading for each pair of aneuploidies. ad, axial diffusivity; alff, amplitude of low-frequency fluctuation; curvind, intrinsic curvature index; foldind, folding index; gauscurv, gaussian curvature; md, mean diffusivity; meancurv, mean curvature; PC, principal component; rd, radial diffusivity; reho, regional homogeneity.

qualitative similarities, with all aneuploidy PC1 maps having high scores in perisylvian cortices and low scores in medial occipital regions (Figure 3B). Quantitatively, the cross-ROI correlation in PC1 scores (Figure 3B, D) and the cross-feature correlation in PC1 loadings (Figure 3C, E) varied substantially between aneuploidy pairs, being most similar between XXY and XYY (scores $r = 0.73$, loadings $r = 0.95$) and least similar between T21 and the sex chromosome aneuploidies (between XXY and T21: scores $r = 0.24$, loadings $r = 0.33$; between XYY and T21: scores $r = 0.30$, loadings $r = 0.54$) (Figure 3C). We focus here on PC1 of multimodal change in each aneuploidy, but subsequent PCs up to a cumulative variance explained of 85% are shown in Figure S5A, B. These components of multimodal change were generally less consistent between aneuploidies than PC1 in their spatial distributions (Figure S5C); however, a given

pattern of feature loadings could connect disparate PCs across aneuploidies (Figure S5D).

Thus, in each aneuploidy approximately, one-third of the spatial variation in 15 ΔIDP across the cortex can be explained by a single principal spatial component which emphasizes morphometric (sMRI-based) and microstructural (DWI-based) measures. This spatial component is positively correlated—but not identical—between aneuploidies: it shows stronger similarity between XXY and XYY in both regional scores and feature loadings, but weak to moderate similarity between the 2 sex chromosome aneuploidies and T21. Moreover, each aneuploidy shows several spatial components of multimodal cortical change beyond PC1, and these tend to be highly dissimilar across the aneuploidies. These results indicate that GDDs differ greatly from each other in the full profile of their effects on human cortical anatomy but share a moderately to strongly correlated PC1 of multimodal cortical change (detailed further below).

Convergent Multimodal Cortical Changes Across Aneuploidies and Links to Convergence Across Behaviorally Defined Disorders

Having defined positively correlated PC1s of multimodal cortical change between aneuploidies, we averaged regional PC1 scores to provide a single summary map of human cortical vulnerability to aneuploidy. This cross-aneuploidy average PC1 map highlighted the insula and ventromedial prefrontal cortex (high average PC1) as well as the occipitoparietal cortices (low average PC1) as regions of core cortical vulnerability (Figure 4A). These regions of convergent vulnerability could also be identified through a complementary conjunction analysis of PC1 deciles (Methods and Materials) (Figure 4B), which also flagged the temporoparietal junction and regions of the lateral prefrontal cortex as areas of relative resilience or inconsistent vulnerability across aneuploidies. Because sMRI-derived cortical volume measures consistently showed strong negative loadings on PC1 for all 3 aneuploidies, the shared axis of cortical vulnerabilities captured by the cross-aneuploidy PC1 map (Figure 4A, B) is therefore largely driven by a shared tendency of aneuploidy to cause a relative reduction of cortical volume in insular and ventromedial prefrontal regions and a relative increase of cortical volume in occipitoparietal regions.

Topographic annotation of the cross-aneuploidy average PC1 map using spin tests revealed a significant omnibus alignment with functional connectivity networks of the cortex defined by the Yeo-Krienen-17 parcellation (28) ($p_{spin} < .05$) (Figure S7A) but not cytoarchitecture parcellations defined by von Economo (27) (Methods and Materials). Post hoc tests identified significant enrichment of high average PC1 scores in the Yeo-Krienen somatomotor and ventral attention subnetworks (Figure 4C). Notably, these networks did not show significant enrichment in individual analyses of each aneuploidy-specific PC1 map, which each had their own pattern of significant overlaps with functional connectivity and cytoarchitectonic parcellations (Figure S8B, D).

Finally, given that all 3 of the aneuploidies included in our study can increase risk for multiple BDDs (5,11) and that previous work has hinted at a shared spatial pattern of cortical vulnerability to multiple BDDs (30,31), we tested for overlap between shared GDD and BDD effects on human cortical anatomy. PC1 of cortical change from measures of CT and SA change in diverse BDDs from the ENIGMA dataset (ENIGMA-PC1, Methods and Materials) showed a moderate-to-strong correlation with the average aneuploidy PC1 map ($R = 0.58$, $p_{spin} = .0005$) (Figure 4D), indicating the existence of a core spatial axis of human cortical vulnerability to diverse genetically and behaviorally defined neuropsychiatric disorders (the same correlation was $R = 0.47$, $p_{spin} = .002$ using an aneuploidy-PC1 map based on SA and CT alone to mirror use of SA and CT in BDD map) (Figure S10). To characterize the biological properties of this spatial axis, we aligned the average PC1 map in aneuploidy to the Allen Human Brain Atlas (32) and used ensemble-based gene category enrichment analysis to quantify associations between the Allen Human Brain Atlas genes' spatial expression and the average PC1 map in aneuploidy (32–34) (see Methods and Materials and the Supplement). Salient biological processes and cell-type marker gene sets enriched among genes expressed along the aneuploidy-PC1 (Figure 4E, F; and Table S4) included the following: negatively correlated with PC1: multiciliated epithelial cell differentiation (cScorePheno = 0.21, $q_{FDR} = 0$) and positive regulation of neuron maturation (cScorePheno = 0.2, $q_{FDR} = 0$); positively correlated with PC1: regulation of serotonin secretion (GO:0014062; cScorePheno = 0.34, $q_{FDR} = .047$) and inhibitory interneurons In1 subtype (cScorePheno = 0.46, $q_{FDR} = .008$).

Stability of Findings With and Without TTV Correction

As a supplementary analysis, we evaluated the difference between the ΔIDP maps with and without correction for TTV (Figures S2A, S3A, and S4A). Spatial correlations between each TTV-corrected ΔIDP map and their TTV-uncorrected counterparts were strong (mean $r = 0.94$, range: 0.87–0.99), indicating that the ranking of cortical regions in each ΔIDP map was not substantially altered by exclusion or inclusion of TTV as a covariate when calculating ΔIDP (Figure S4B). Accordingly, we also observed substantial consistency between TTV-corrected and uncorrected analyses for organizing principles of the 45 × 45 ΔIDP correlation matrix (Figure S4C, D), aneuploidy-specific PC regional scores and feature loadings (Figures S5 and S6A–C), the aneuploidy PC1 maps (for each aneuploidy and on average) and their alignments with Yeo-Krienen-17 (Figures S6D–F and S7), and von Economo parcellations (Figures S7 and S8C, E).

DISCUSSION

Our study provides an unprecedentedly deep phenotypic analysis of neuroimaging changes in multiple GDDs by examining multimodal neuroimaging data in 3 different aneuploidy syndromes. This enriched dataset advances understanding of each individual aneuploidy considered, reveals organizing principles for regional cortical change across aneuploidies, localizes cortical regions with shared vulnerability across aneuploidies, and shows that shared cortical

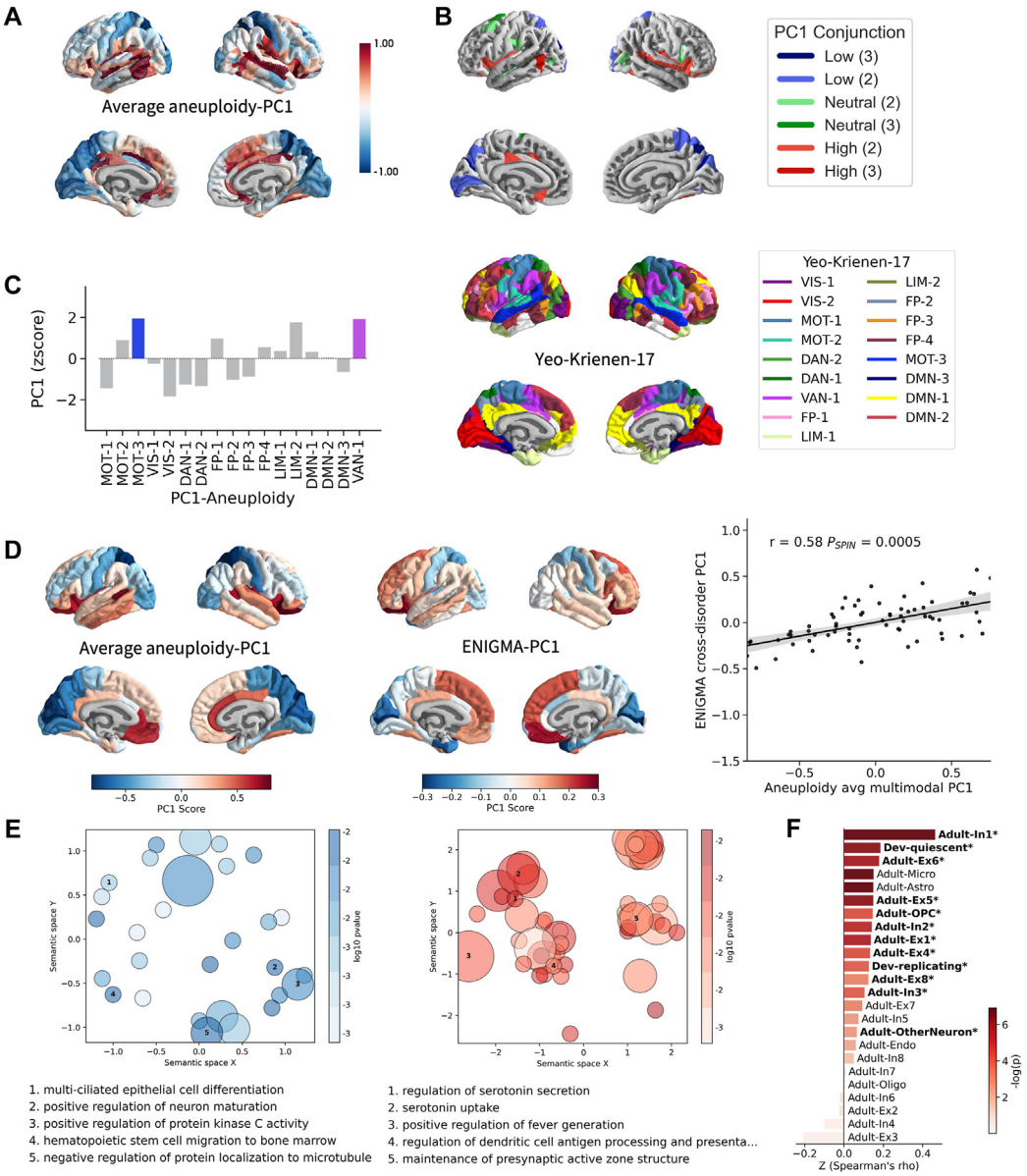

Figure 4. Defining and characterizing convergent regional vulnerability of the human cortex. **(A)** Average first principal component (PC1) map (Aneuploidy-PC1) projected onto the cortical surface (in the HCP [Human Connectome Project]/Glasser atlas parcellation). **(B)** Conjunction map showing regions of interest which sit at the top (reds), middle (greens), and bottom (blues) deciles of PC1 scores across aneuploidy/gene dosage disorders. **(C)** Enrichment of functional connectivity modules defined by Yeo-Krienen-17 (top cortical surfaces, mapped to the Glasser parcellation) for extreme PC1 scores within the Aneuploidy-PC1 map. **(D)** On the left, we show the average aneuploidy PC1 map re-parcellated using the Desikan-Killiany atlas (see Methods and Materials). In the middle, we show the PC1 map generated from applying principal component analysis to case-control surface area and cortical thickness maps from behaviorally defined psychiatric disorders in the ENIGMA dataset (ENIGMA-PC1). On the right, we show the spatial correlation between the Aneuploidy-PC1 map and the ENIGMA-PC1 map. **(E)** We show the gene ontology biological processes' gene category enrichment analysis results for the Aneuploidy-PC1 map. The 2 panels are color coded in red and blue, with red denoting categories that are significantly enriched for the high end of the PC1 map and blue denoting categories that are enriched for the low end of the PC1 map. Each circle represents a cluster of gene ontology categories, with the point size representing the number of categories in a cluster and point color representing the uncorrected *p* values derived after fitting a standard distribution to the permutation-derived null category scores. Clusters are sorted by the cScorePheno scores. Only categories that remained significant after false discovery rate correction are included here. **(F)** Cell-type enrichment analysis using bars that represent category scores; the color reflects the negative base 10 logarithm of the uncorrected *p* values; asterisks and bolding represent cell types that survived false discovery rate correction. DAN, dorsal attention network; DMN, default mode network; ENIGMA, Enhancing Neuro Imaging Genetics through Meta Analysis; FP, frontoparietal; LIM, limbic; MOT, somatomotor; OPC, oligodendrocyte progenitor cell; VAN, ventral attention network; VIS, visual.

changes across these GDDs are correlated with shared cortical changes across BDDs. We consider each implication of our study findings in further detail below.

Most previous neuroimaging studies of XXY, XYY, and T21 have examined changes in GMV, CT, and SA, and we replicated these previously reported findings while also revealing new patterns of cortical vulnerability by extending the scope of our analysis beyond sMRI phenotypes. Salient examples include increased diffusivity in the temporal cortex and decreased diffusivity in the cingulate cortex for XXY, which may reflect altered myelin integrity, and reduced ALFF in the inferior frontal cortex for XXY and XYY, which may reflect reduced activity or hypoactivation while at rest (35). We found a statistically significant increase in anisotropy in the auditory association cortex for T21 [but see (36)]. We note that the sparse statistically significant effects detected for DWI and rs-fMRI as compared with sMRI, despite similar effect sizes, likely reflects modality differences in available sample size (motivating future work in similarly large sample sizes for all modalities across different GDDs). Nevertheless, the diversity of regional changes observed across the different cortical phenotypes and aneuploidies examined here implies highly variegated mechanisms for regional cortical change in each aneuploidy (and shows how this complexity is missed by focusing on the most commonly measured sMRI phenotype alone).

By systematically comparing the spatial pattern of cortical change for all aneuploidy-phenotype combinations, our study suggests that the patterning of cortical change in GDDs may primarily vary by imaging modality and then by GDD subtype within modality. Different spatial patterns of brain change from sMRI and rs-fMRI have also been reported in murine GDD models (37,38). High spatial correlations across phenotypes derived from the same modality may reflect shared genetic architectures between imaging features that capture similar tissue properties (39) but may also reflect modality-specific sources of methodological variance. However, we also observe that regional cortical changes vary by aneuploidy type within each conjointly altered set of phenotypes, pointing to gene-set–specific effects. Indeed, even among aneuploidies that alter the dosage of large gene sets with a theoretically greater potential for overlapping effects, we still observe differentiable spatial patterns of cortical change by aneuploidy type. We speculate that the greater sharing of effects between XXY and XYY as compared with between either of these sex chromosome aneuploidies and trisomy 21 may reflect shared gene sets between the X- and Y-chromosome that are not present on chromosome 21, including pseudoautosomal genes and X-Y gametolog pairs (40,41).

Lastly, we used PCA to show that while each aneuploidy induces a unique constellation of cortical change across different imaging features and cortical regions, there is some commonality between aneuploidies in PC1 of multimodal cortical change. Given observed PC feature loadings, convergent cortical vulnerability to aneuploidy was largely driven by relative volume reductions in ventral attention systems alongside relative volume increases in somatomotor networks. We found that this spatial axis of shared cortical vulnerability to aneuploidy is partially aligned with the shared spatial axis of cortical vulnerability across multiple BDDs (31). This observation suggests that diverse risk factors for neuropsychiatric illness can converge to modify cortical organization along a similar spatial axis. Transcriptional and functional gene-set enrichment analyses associated with this axis include serotonergic signaling and marker genes for an inhibitory interneuron cell class (In1), both of which have been implicated in the biology of psychiatric disorders that appear at increased rates in aneuploidy syndromes (31,42,43). However, we note that these findings and interpretation are based only on PC1 of cortical change in each aneuploidy, which captures only a fraction of all multimodal signals. Additional signatures of multimodal change may align with other molecular and cellular processes.

Our findings must be considered in light of several caveats and limitations. First, although we included substantially more IDPs than were previously studied in multiple GDDs, future work needs to expand even further on the set of phenotypes studied and include other GDDs. Second, our cross-sectional study design did not allow us to capture how cortical changes may unfold developmentally as they relate to either individual aneuploidies or shared mechanisms. Relatedly, the Allen Human Brain Atlas analysis makes use of gene expression data in adults, so it may miss molecular and cellular mechanisms that are specific to atypical cortical organization in early development. In addition, although GDDs are primarily defined as disorders of gene dosage, we acknowledge that their impacts may also reflect dosage alteration of regulatory intergenic regions and are realized through mechanistically complex downstream changes across numerous aspects of biological structure and function. Finally, it remains an open question whether variation in multimodal changes among carriers of the same GDD relate to variation in co-occurring cognitive and behavioral symptoms. Given that the relative rarity of GDDs limits sample sizes, detection of brain-behavior associations in GDDs will likely be feasible only if the strength of such associations in GDDs is stronger than those that have been reported recently in genetically unselected groups (44).

Notwithstanding the above limitations, our study secures a more comprehensive picture of cortical alterations across 3 distinct aneuploidies and emphasizes a shared backbone of cortical vulnerability amid the diversity of effects for different IDPs in different GDDs. Strikingly, this shared signature of cortical vulnerability to aneuploidy is consistent with the shared signature of cortical change among diverse behaviorally defined disorders that occur at elevated rates in aneuploidies and other GDDs. The cortical gradient revealed by these shared effects represents a high-priority target for future translational research in basic and clinical neuroscience.

ACKNOWLEDGMENTS AND DISCLOSURES

This study was supported by the Intramural Research Program of the National Institute of Mental Health (project funding: Grant No. 1ZIAMH002949-03 [to AR]; ClinicalTrials.gov identifier: NCT00001246; protocol: 89-M-0006).

EL, DCA and AR conceptualized the study and wrote original draft; EL, DCA, and AR administered the project; EL, SL, DCA, and AR contributed to methodology, software, and formal analysis; EL performed visualization; ETW, AW, ET, LSC, JB, FML, and JS collected data; AR acquired funds; all authors wrote, reviewed and edited the manuscript; and DCA and AR supervised the study.

We thank all the participants and their families for their generous involvement in this study. We acknowledge members of the University College London's Progression Of Neurodegenerative Disease group (http://pond.cs.ucl.ac.uk) for feedback and input received during group discussions.

A previous version of this article was published as a preprint on bioRxiv: https://www.biorxiv.org/content/10.1101/2022.11.12.516252v1.abstract.

All analyses have been made available at https://github.com/llevitis/NIH_Multimodal_Aneuploidy_Phenotypes. Further information and requests for resources should be directed to Dr. Armin Raznahan (raznahana@mail.nih.gov).

The authors report no biomedical financial interests or potential conflicts of interest.

ARTICLE INFORMATION

From the Section on Developmental Neurogenomics, National Institute of Mental Health, Bethesda, Maryland (EL, SL, ETW, AW, ET, LSC, FML, AR); Center for Medical Image Computing, Department of Computer Science, UCL, London, UK (EL, DCA); and National Institutes of Health MRI Research Facility, National Institute of Mental Health, Bethesda, Maryland (JS).

Address correspondence to Elizabeth Levitis, M.Sc., at elizabeth.levitis@nih.gov, or Armin Raznahan, M.D., Ph.D., at raznahana@mail.nih.gov.

Received Feb 1, 2023; revised Jun 16, 2023; accepted Jul 10, 2023.

Supplementary material cited in this article is available online at https://doi.org/10.1016/j.biopsych.2023.07.008.

REFERENCES

1. Raznahan A, Lee NR, Greenstein D, Wallace GL, Blumenthal JD, Clasen LS, Giedd JN (2016): Globally divergent but locally convergent X- and Y-chromosome influences on cortical development. Cereb Cortex 26:70–79.
2. Moreau CA, Urchs SGW, Kuldeep K, Orban P, Schramm C, Dumas G, *et al.* (2020): Mutations associated with neuropsychiatric conditions delineate functional brain connectivity dimensions contributing to autism and schizophrenia. Nat Commun 11:5272.
3. Seidlitz J, Nadig A, Liu S, Bethlehem RAI, Vértes PE, Morgan SE, *et al.* (2020): Transcriptomic and cellular decoding of regional brain vulnerability to neurogenetic disorders. Nat Commun 11:3358.
4. Modenato C, Kumar K, Moreau C, Martin-Brevet S, Huguet G, Schramm C, *et al.* (2021): Effects of eight neuropsychiatric copy number variants on human brain structure. Transl Psychiatry 11:399.
5. Rau S, Whitman ET, Schauder K, Gogate N, Lee NR, Kenworthy L, Raznahan A (2021): Patterns of psychopathology and cognition in sex chromosome aneuploidy. J Neurodev Disord 13:61.
6. Whitman ET, Liu S, Torres E, Warling A, Wilson K, Nadig A, *et al.* (2021): Resting-state functional connectivity and psychopathology in Klinefelter syndrome (47, XXY). Cereb Cortex 31:4180–4190.
7. Lepage JF, Hong DS, Raman M, Marzelli M, Roeltgen DP, Lai S, *et al.* (2014): Brain morphology in children with 47, XYY syndrome: A voxel- and surface-based morphometric study. Genes Brain Behav 13:127–134.
8. Lee NR, Adeyemi EI, Lin A, Clasen LS, Lalonde FM, Condon E, *et al.* (2016): Dissociations in cortical morphometry in youth with Down syndrome: Evidence for reduced surface area but increased thickness. Cereb Cortex 26:2982–2990.
9. Hamner T, Udhnani MD, Osipowicz KZ, Lee NR (2018): Pediatric brain development in Down syndrome: A field in its infancy. J Int Neuropsychol Soc 24:966–976.
10. Nielsen J, Wohlert M (1991): Chromosome abnormalities found among 34,910 newborn children: Results from a 13-year incidence study in Arhus, Denmark. Hum Genet 87:81–83.
11. Vicari S (2006): Motor development and neuropsychological patterns in persons with Down syndrome. Behav Genet 36:355–364.
12. Glasser MF, Coalson TS, Robinson EC, Hacker CD, Harwell J, Yacoub E, *et al.* (2016): A multi-modal parcellation of human cerebral cortex. Nature 536:171–178.
13. Rosen AFG, Roalf DR, Ruparel K, Blake J, Seelaus K, Villa LP, *et al.* (2018): Quantitative assessment of structural image quality. NeuroImage 169:407–418.
14. Chamberland M, Raven EP, Genc S, Duffy K, Descoteaux M, Parker GD, *et al.* (2019): Dimensionality reduction of diffusion MRI measures for improved tractometry of the human brain. Neuroimage 200:89–100.
15. Theaud G, Houde JC, Boré A, Rheault F, Morency F, Descoteaux M (2020): TractoFlow: A robust, efficient and reproducible diffusion MRI pipeline leveraging Nextflow & Singularity. Neuroimage 218:116889.
16. Gorgolewski K, Burns CD, Madison C, Clark D, Halchenko YO, Waskom ML, Ghosh SS (2011): Nipype: A flexible, lightweight and extensible neuroimaging data processing framework in python. Front Neuroinform 5:13.
17. Esteban O, Markiewicz CJ, Burns C, Goncalves M, Jarecka D, Ziegler E, et al. (2021): nipy/nipype: 1.7.0, version 1.7.0. Zenodo. Available at: https://doi.org/10.5281/zenodo.5585697. Accessed November 3, 2021.
18. Esteban O, Markiewicz CJ, Blair RW, Moodie CA, Isik AI, Erramuzpe A, *et al.* (2019): fMRIPrep: A robust preprocessing pipeline for functional MRI. Nat Methods 16:111–116.
19. Ciric R, Rosen AFG, Erus G, Cieslak M, Adebimpe A, Cook PA, *et al.* (2018): Mitigating head motion artifact in functional connectivity MRI. Nat Protoc 13:2801–2826.
20. Jezzard P, Balaban RS (1995): Correction for geometric distortion in echo planar images from B0 field variations. Magn Reson Med 34:65–73.
21. Norris DG, Zysset S, Mildner T, Wiggins CJ (2002): An investigation of the value of spin-echo-based fMRI using a Stroop color-word matching task and EPI at 3 T. NeuroImage 15:719–726.
22. Williams CM, Peyre H, Toro R, Ramus F (2021): Neuroanatomical norms in the UK Biobank: The impact of allometric scaling, sex, and age. Hum Brain Mapp 42:4623–4642.
23. Warling A, McDermott CL, Liu S, Seidlitz J, Rodrigue AL, Nadig A, *et al.* (2021): Regional white matter scaling in the human brain. J Neurosci 41:7015–7028.
24. Alexander-Bloch A, Giedd JN, Bullmore E (2013): Imaging structural co-variance between human brain regions. Nat Rev Neurosci 14:322–336.
25. Váša F, Seidlitz J, Romero-Garcia R, Whitaker KJ, Rosenthal G, Vértes PE, *et al.* (2018): Adolescent tuning of association cortex in human structural brain networks. Cereb Cortex 28:281–294.
26. von Economo CF, Koskinas GN (1925): Die Cytoarchitektonik der Hirnrinde des Erwachsenen Menschen. Berlin: Springer.
27. Scholtens LH, de Reus MA, de Lange SC, Schmidt R, van den Heuvel MP (2018): An MRI von Economo – Koskinas atlas. Neuroimage 170:249–256.
28. Yeo BT, Krienen FM, Sepulcre J, Sabuncu MR, Lashkari D, Hollinshead M, *et al.* (2011): The organization of the human cerebral cortex estimated by intrinsic functional connectivity. J Neurophysiol 106:1125–1165.
29. Larivière S, Paquola C, Park BY, Royer J, Wang Y, Benkarim O, *et al.* (2021): The ENIGMA Toolbox: Multiscale neural contextualization of multisite neuroimaging datasets. Nat Methods 18:698–700.
30. Opel N, Goltermann J, Hermesdorf M, Berger K, Baune BT, Dannlowski U (2020): Cross-disorder analysis of brain structural abnormalities in six major psychiatric disorders: A secondary analysis of mega- and meta-analytical findings from the ENIGMA consortium. Biol Psychiatry 88:678–686.
31. Park BY, Kebets V, Larivière S, Hettwer MD, Paquola C, van Rooij D, *et al.* (2022): Multiscale neural gradients reflect transdiagnostic effects of major psychiatric conditions on cortical morphology. Commun Biol 5:1024.
32. Hawrylycz M, Miller JA, Menon V, Feng D, Dolbeare T, Guillozet-Bongaarts AL, *et al.* (2015): Canonical genetic signatures of the adult human brain. Nat Neurosci 18:1832–1844.
33. Fulcher BD, Arnatkeviciute A, Fornito A (2021): Overcoming false-positive gene-category enrichment in the analysis of

spatially resolved transcriptomic brain atlas data. Nat Commun 12:2669.

34. Lotter LD, Dukart J, Fulcher BD (2022): ABAnnotate: A toolbox for ensemble-based multimodal gene-category enrichment analysis of human neuroimaging data. version v.0.1.0. Zenodo. Available at: https://doi.org/10.5281/zenodo.6463329. Accessed ●●●.
35. Aiello M, Salvatore E, Cachia A, Pappatà S, Cavaliere C, Prinster A, *et al.* (2015): Relationship between simultaneously acquired resting-state regional cerebral glucose metabolism and functional MRI: A PET/MR hybrid scanner study. Neuroimage 113:111–121.
36. Lee NR, Nayak A, Irfanoglu MO, Sadeghi N, Stoodley CJ, Adeyemi E, *et al.* (2020): Hypoplasia of cerebellar afferent networks in Down syndrome revealed by DTI-driven tensor based morphometry. Sci Rep 10:5447.
37. Ellegood J, Anagnostou E, Babineau BA, Crawley JN, Lin L, Genestine M, *et al.* (2015): Clustering autism: Using neuroanatomical differences in 26 mouse models to gain insight into the heterogeneity. Mol Psychiatry 20:118–125.
38. Zerbi V, Pagani M, Markicevic M, Matteoli M, Pozzi D, Fagiolini M, *et al.* (2021): Brain mapping across 16 autism mouse models reveals a spectrum of functional connectivity subtypes. Mol Psychiatry 26:7610–7620.
39. van der Meer D, Frei O, Kaufmann T, Shadrin AA, Devor A, Smeland OB, *et al.* (2020): Understanding the genetic determinants of the brain with MOSTest. Nat Commun 11:3512.
40. Raznahan A, Parikshak NN, Chandran V, Blumenthal JD, Clasen LS, Alexander-Bloch AF, *et al.* (2018): Sex-chromosome dosage effects on gene expression in humans. Proc Natl Acad Sci U S A 115:7398–7403.
41. Liu S, Akula N, Reardon PK, Russ J, Torres E, Clasen LS, *et al.* (2023): Aneuploidy effects on human gene expression across three cell types. Proc Natl Acad Sci U S A 120:e2218478120.
42. Marazziti D (2017): Understanding the role of serotonin in psychiatric diseases. F1000Res 6:180.
43. Wang P, Zhao D, Lachman HM, Zheng D (2018): Enriched expression of genes associated with autism spectrum disorders in human inhibitory neurons. Transl Psychiatry 8:13.
44. Marek S, Tervo-Clemmens B, Calabro FJ, Montez DF, Kay BP, Hatoum AS, *et al.* (2022): Reproducible brain-wide association studies require thousands of individuals. Naature 603:654–660.